

This work was written as part of one of the author's official duties as an Employee of the United States Government and is therefore a work of the United States Government. In accordance with 17 U.S.C. 105, no copyright protection is available for such works under U.S. Law.

Public Domain Mark 1.0

<https://creativecommons.org/publicdomain/mark/1.0/>

Access to this work was provided by the University of Maryland, Baltimore County (UMBC) ScholarWorks@UMBC digital repository on the Maryland Shared Open Access (MD-SOAR) platform.

**Please provide feedback**

Please support the ScholarWorks@UMBC repository by emailing [scholarworks-group@umbc.edu](mailto:scholarworks-group@umbc.edu) and telling us what having access to this work means to you and why it's important to you. Thank you.

# Kalman Filtering Approach to Multispectral/Hyperspectral Image Classification

CHEIN-I CHANG, Senior Member, IEEE  
CLARK BRUMBLEY

Linear unmixing is a widely used remote sensing image processing technique for subpixel classification and detection where a scene pixel is generally modeled by a linear mixture of spectral signatures of materials present within the pixel. An approach, called linear unmixing Kalman filtering (LUKF), is presented which incorporates the concept of linear unmixing into Kalman filtering so as to achieve signature abundance estimation, subpixel detection and classification for remotely sensed images. In this case, the linear mixture model used in linear unmixing is implemented as the measurement equation in Kalman filtering. The state equation which is required for Kalman filtering but absent in linear unmixing is then used to model the signature abundance. By utilizing these two equations the proposed LUKF not only can detect abrupt change in various signature abundances within pixels, but also can detect and classify desired target signatures. The performance of effectiveness and robustness of the LUKF is demonstrated through simulated data and real scene images, Satellite Pour l'Observation de la Terra (SPOT) and Hyperspectral Digital Imagery Collection (HYDICE) data.

Manuscript received November 22, 1997.

IEEE Log No. T-AES/35/1/01509.

Authors' current addresses: C.-I Chang, Remote Sensing Signal and Image Processing Laboratory, Dept. of Computer Science and Electrical Engineering, University of Maryland Baltimore County, 1000 Hilltop Circle, Baltimore, MD 21250; C. Brumbley, Dept. of Defense, Ft. Meade, MD.

0018-9251/99/\$10.00 © 1999 IEEE

## I. INTRODUCTION

Remotely sensed images have been used in a broad range of applications ranging from geology, agriculture, and global change detection to defense and law enforcement [1]. They are generally acquired by multiple-band sensors operated from either a spaceborne or an airborne platform. Examples include satellite multispectral sensors such as Landsat 7-band Thematic Mapper (TM), 4-band Multispectral Scanner (MSS), 3-band SPOT (Satellite Pour l'Observation de la Terra) and airborne hyperspectral sensors such as the 224-band NASA Jet Propulsion Laboratory's Airborne Visible/Infrared Imaging Spectrometer (AVIRIS) and the 210-band Naval Research Laboratory's Hyperspectral Digital Imagery Collection (HYDICE). Since the area covered by a multispectral/hyperspectral image pixel is generally 20–30 m by 20–30 m (except HYDICE data which has spatial resolution ranging from 1 m to 4 m), a scene pixel usually contains more than one material and results in a mixture of these materials. One of the major challenges in remote sensing data exploitation is to discriminate, quantify, and identify multiple material constituents in a mixed pixel. In particular, when the size of a target is smaller than the ground sampling distance, detecting such a target at subpixel scale presents great difficulty because the target is embedded in only one pixel and cannot be seen from the image.

Linear unmixing has been a widely used technique to unmix multicomponent mixtures [2, 3, 4]. It models a pixel as a linear mixture of spectral signatures of materials within that pixel, then inverts the signature matrix formed by the spectra of the materials to identify and classify these individual material components in the pixel. Unfortunately, it works only on a pixel-by-pixel basis and does not take into account the pixel spatial correlation. Therefore, it cannot detect the change in the abundance vector from one pixel to another. Kalman filtering is a well-known technique in control, communications, and signal processing and has been used in versatile applications because it can be implemented recursively in real-time data processing as well as for nonstationary data. By taking advantage of strengths of the Kalman filtering, an approach based on a concept of combining the Kalman filtering and linear unmixing, called linear unmixing Kalman filtering (LUKF) is introduced for subpixel detection and classification for remotely sensed images. The LUKF can be also be viewed as a hybrid of the linear unmixing and the Kalman filtering which implements the linear unmixing in a Kalman filtering fashion. More specifically, the measurement (also referred to as observation, output or process) equation required for the Kalman filter is governed by the linear mixture model while the state equation of the Kalman filter is used as an ancillary equation for

the linear unmixing to describe the state of signature abundance. These equations are corrupted by two zero mean and uncorrelated noise processes. Each covariance matrix is modeled by the identity matrix multiplied by a scalar. These two scalar variances are important parameters and affect the performance of the LUKF. Their effects on the performance is demonstrated through computer simulations and real data. The measurement noise variance  $\sigma_u^2$  is the noise component of the signal-to-noise ratio (SNR) of the input data and in general is not known *a priori*. The state noise  $\sigma_v^2$  controls the amount of change in the abundance from pixel to pixel. The LUKF is applied to simulated data over a range of values for these parameters to determine their effects. These values are then used in the LUKF for real scene data. Two types of real data are conducted for experiment, multispectral image data-SPOT images and hyperspectral image data-HYDICE images. The results show the robustness of the LUKF to changes in the two parameters of the model,  $\sigma_u^2$  and  $\sigma_v^2$ .

The remainder of the paper is organized as follows. Section II describes the linear mixture model used in the linear unmixing. Section III briefly describes the Kalman filter in conjunction with the linear unmixing and its application to signature abundance estimation. Section IV presents the results of test run on simulated hyperspectral and multispectral data. Section V applies the LUKF to HYDICE and SPOT data to demonstrate the performance. Section VI draws a brief conclusion.

## II. LINEAR MIXTURE MODEL

A hyperspectral image cube is made up of many, usually hundreds, of images that are spatially co-registered. Each of these images represents the reflected energy of the materials within the pixel at different wavelengths and bandwidths. For example, the HYDICE sensor has 210 bands that collect reflected energy in the ranges of 0.4 to 2.5  $\mu\text{m}$ . These spatially co-registered pixels can be combined into a vector representing the spectral signatures of the materials within the pixel.

The area covered by an individual pixel usually contains several different materials that have different spectral signatures. When the area of the pixel contains more than one material, the pixel is a combination of the different spectral signatures of the materials. Such pixels are referred to as mixed pixels. Linear unmixing is one of many techniques used in hyperspectral/multispectral image classification and is used here to describe the image pixels. This method assumes that each image pixel is linearly mixed by the spectral signatures of the materials contained in the pixel. Let the vector  $\mathbf{r}(x,y)$  denote the image pixel at the location  $(x,y)$ . This pixel vector is of dimension  $N$  by 1 where  $N$  is the number of bands

in the image. Next define an  $N$  by  $M$  signature matrix  $\mathbf{S}$  as  $(s_1, s_2 \dots s_M)$ . The vector  $s_i$  is an  $N$  by 1 column vector representing the spectral signature of the  $i$ th material. Finally define an  $M$  by 1 abundance vector  $\mathbf{a}(x,y)$  denoted by  $[a_1(x,y), a_2(x,y), \dots, a_M(x,y)]^T$  where  $a_i(x,y)$  represents the abundance of the  $i$ th material in the pixel at location  $(x,y)$ . A linear mixture model is then given by (1)

$$\mathbf{r}(x,y) = \mathbf{S}\mathbf{a}(x,y) + \mathbf{u}(x,y) \quad (1)$$

where the signature matrix  $\mathbf{S}$  is assumed to be invariant to spatial location and the  $N$  by 1 vector  $\mathbf{u}(x,y)$  represents white additive noise with zero mean and covariance matrix given by  $\sigma_u^2 \mathbf{I}_N$ . The matrix  $\mathbf{I}_N$  is the  $N$  by  $N$  identity matrix. Subpixel image classification identifies materials present in a mixed pixel at the subpixel scale based on the value of  $\mathbf{a}(x,y)$  given  $\mathbf{r}(x,y)$  and the signature matrices.

## III. KALMAN FILTERING

This section presents a description of the Kalman filter and the steps taken to perform Kalman filtering. A complete derivation based on the innovations approach is presented in Haykin [9]. Kalman filtering is a minimum mean-squared estimator and has two distinct features. The first of these features is that Kalman filtering is based on state-space concept. This feature allows Kalman filtering to process the system as a whole unit as opposed to a group of individual components. The second of these features is that Kalman filtering is recursive. The update of the estimate of the state is computed from the current estimate and the current input data. This property makes Kalman filtering more efficient than computing the estimate from the entire past input data at each step of the filtering process. The Kalman filter does no more work processing the hundredth input sample as it did for the first input sample. This recursive feature also eliminates the need to store all previous input data and previous state estimates.

The application of the linear unmixing to Kalman filtering was first proposed in C. Brumbley and C.-I Chang [6]. The idea of Kalman filter is relatively simple. First, assume that you have a system that is described by its state vector  $\mathbf{a}(n)$ . In our case, the state vector is the signature abundance vector. We cannot observe the state vector directly, but we do have observation data  $\mathbf{r}(n)$  that is corrupted by noise  $\mathbf{u}(n)$ . This observation data is related to the state of the system by the measurement equation that is given by linear mixture model, (1)

$$\mathbf{r}(n) = \mathbf{S}\mathbf{a}(n) + \mathbf{u}(n). \quad (2)$$

The index  $n$  is used instead of  $(x,y)$  to represent the pixel to be processed at the time  $n$ . The  $N$  by  $M$  measurement matrix  $\mathbf{S}$  represents the relationship between the observed data and the state vector and

is the signature matrix in (1). The measurement noise vector is assumed to be zero-mean, white process with correlation matrix given by (3)

$$E[\mathbf{u}(n)\mathbf{u}^T(k)] = \mathbf{R}\delta_{nk} = \sigma_u^2 \mathbf{I}_N \delta_{nk}. \quad (3)$$

where  $\mathbf{I}_N$  is the  $N$  by  $N$  identity matrix and  $\delta_{nk}$  is Kronecker's notation given by  $\delta_{nk} = 1$  if  $n = k$  and  $\delta_{nk} = 0$  if  $n \neq k$ . In order to perform Kalman filtering a state equation is required. This equation must relate the current state of the system  $\mathbf{a}(n)$  to the previous state  $\mathbf{a}(n-1)$ . This equation is called the abundance equation in this work and is assumed to be linear with an additive noise term. The abundance equation is given in (4)

$$\mathbf{a}(n+1) = \Phi(n+1, n)\mathbf{a}(n) + \mathbf{v}(n). \quad (4)$$

The known  $M$  by  $M$  state transition matrix  $\Phi(n+1, n)$  relates the state of the system at time  $n$  to time  $n+1$ . A Gauss–Markov model is used to model this relationship. Here we assume that  $\Phi(n+1, n) = \mathbf{I}$  is an identity matrix. This means the  $j$ th abundance  $\mathbf{a}_j(n+1)$  at time  $n+1$  is predicted solely on the abundance  $\mathbf{a}_j(n)$  of the immediate past pixel. This type of prediction is generally referred to as the zero-order holder interpolation used in predictive coding such as differential pulse code modulation (DPCM) in communications, signal, and image processing. The process noise vector  $\mathbf{v}(n)$  is assumed to be a zero-mean, white process with correlation equation given by (5)

$$E[\mathbf{v}(n)\mathbf{v}^T(k)] = \mathbf{Q}\delta_{nk} = \sigma_v^2 \mathbf{I}_M \delta_{nk} \quad (5)$$

where  $\mathbf{I}_M$  is the  $M$  by  $M$  identity matrix and  $\delta_{nk}$  is Kronecker's notation. The matrix  $\mathbf{I}_M$  represents the  $M$  by  $M$  identity matrix. Since the state transition matrix is assumed to be the identity matrix, the value of  $\sigma_v^2$  controls the amount of change allowed in the abundance vector from one pixel to the next pixel.

The goal of Kalman filtering is to obtain the minimum mean-squared estimate of the abundance state  $\mathbf{a}(k)$ , given that the data  $\mathbf{r}(k)$  is observed. Using the predicted knowledge from  $\mathbf{a}(k)$  we can detect and classify the pixel  $\mathbf{r}(k)$ . Let  $\hat{\mathbf{a}}(k|k-1)$  represent the minimum mean-squared predictor of  $\mathbf{a}(k)$  given the past observations  $\mathbf{r}(j)$  for all  $j$  from one to  $k-1$ .  $\hat{\mathbf{a}}(k|k)$ ,  $\hat{\mathbf{a}}(k|k-1)$ ,  $\mathbf{P}(k|k)$  and  $\mathbf{P}(k+1|k)$  are also defined similarly. The LUKF is performed recursively as follows. For detailed implementation of Kalman filtering, we refer to [9].

*Initial Conditions:*

- 1)  $\mathbf{Q}$  and  $\mathbf{R}$ .
- 2)  $\hat{\mathbf{a}}(0|-1) = \text{mean}[\mathbf{a}(0)] = E[\mathbf{a}(0)]$ .
- 3)  $\mathbf{P}(0|-1) = \text{cov}[\mathbf{a}(0)]$ .

*Measurement Update:*

- 1) Compute Kalman gain at the current time  $k$

$$\mathbf{K}(k) = [\mathbf{P}(k|k-1)\mathbf{S}^T][\mathbf{S}\mathbf{P}(k|k-1)\mathbf{S}^T + \mathbf{R}(k)]^{-1}. \quad (6)$$

- 2) Update the abundance estimate at the current time  $k$  with  $\mathbf{r}(k)$

$$\hat{\mathbf{a}}(k|k) = \hat{\mathbf{a}}(k|k-1) + \mathbf{K}(k)[\mathbf{r}(k) - \mathbf{S}\hat{\mathbf{a}}(k|k-1)]. \quad (7)$$

- 3) Update the error covariance matrix at current time  $k$

$$\mathbf{P}(k|k) = [\mathbf{I} - \mathbf{K}(k)\mathbf{S}]\mathbf{P}(k|k-1). \quad (8)$$

*Abundance Update:*

- 1) Predict the abundance at next time  $k+1$

$$\hat{\mathbf{a}}(k+1|k) = \Phi(k+1, k)\hat{\mathbf{a}}(k|k). \quad (9)$$

- 2) Predict the error covariance matrix at next time  $k+1$

$$\mathbf{P}(k+1|k) = \Phi(k+1, k)\mathbf{P}(k|k)\Phi^T(k+1, k) + \mathbf{Q}. \quad (10)$$

#### IV. COMPUTER SIMULATIONS

Two assumptions were made in modeling the LUKF for subpixel classification. The first of these assumptions was that the mixed pixels can be modeled using a linear mixture model. This is a widely used model in multispectral image classification. The second of these assumptions was that the relationship of the abundance vector between adjacent pixels can be modeled as a Gauss–Markov process. In an agricultural scene, where there are large fields of a single crop, this assumption seems reasonable. This assumption must be tested under conditions where large changes in the abundance vector can occur between adjacent pixels to show that the assumption is valid. The algorithm was run against computer simulated data to test this assumption.

These tests are also used to determine the effects of the unknown parameters  $\sigma_u^2$  and  $\sigma_v^2$ . From (2), the parameter  $\sigma_u^2$  represents the energy of the measurement noise. The measurement noise represents the noise in the image data and can be determined if the SNR of the image is known. This SNR is typically difficult to measure accurately, but good estimates can be obtained easily. These tests show the effects of an inaccurate estimate of measurement noise energy on the performance of the LUKF. If SNR of the simulated data is known, the effects of incorrectly estimating the noise energy of performance can be reduced by adjusting the value of the parameter  $\sigma_u^2$ . The second unknown parameter is the process noise energy  $\sigma_v^2$ . From (4), this parameter represents the energy in the unpredictable part of the change in the state from time  $n$  to  $n+1$ . The relationship of the abundance from one pixel to the next is modeled as a Gauss–Markov process with the state transition matrix being the identity matrix. Thus, this unpredictable component is the only change in the abundance vector between successive states. If the parameter  $\sigma_v^2$  is set

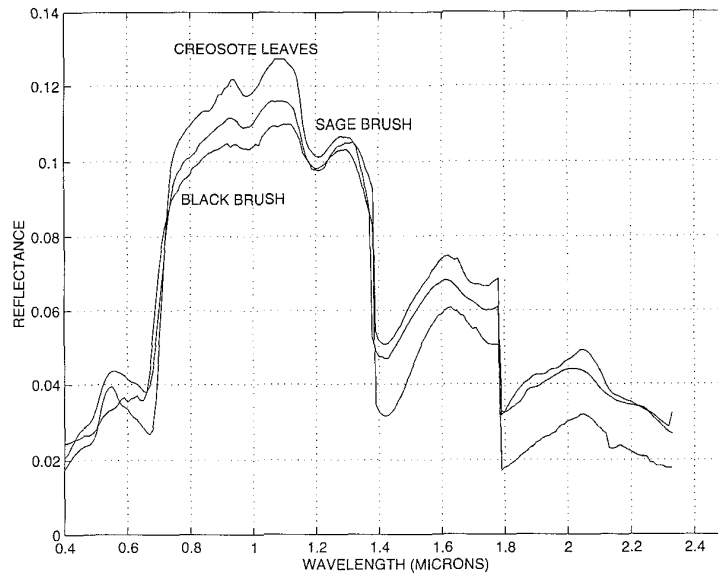


Fig. 1. Reflectances of creosote leaves, sage brush, and black brush from AVIRIS scene.

too low the estimate of the abundance vector will not track small changes in the abundance vector. If it is set too high the estimate will quickly react to sudden changes in the abundance vector but may be driven too much by the measurement noise. This would make the estimate of the abundance vector very noisy and unreliable. The value of  $\sigma_v^2$  is varied to show the effects of this parameter on the performance of the LUKF. The LUKF is applied to both hyperspectral and multispectral data at a known SNR. The parameters  $\sigma_u^2$  and  $\sigma_v^2$  are set to various values and the results used to determine effects of the parameters on the performance of the LUKF. These results are used to determine the range of the two parameters that are acceptable to performance of the LUKF. The Kalman filter was initialized by setting the initial estimate of the abundance vector to zero and the correlation matrix is set to the identity matrix for all the experiments in this work.

#### A. Computer Simulations Using 3 Spectral Reflectances from an AVIRIS Scene

In this section, the results of applying the LUKF to AVIRIS spectral reflectances are presented. The same spectral reflectances that were used in [5] are used in this experiment. This data set consists of the spectral reflectances of creosote leaves, sage brush, and black brush. The three signatures are shown in Fig. 1 and are used because of their similarity. The measure used to determine the similarity of the spectra is called the spectral divergence [10].

The idea of the spectral divergence is to normalize the two spectra  $s_i$  and  $s_j$  so that they sum to unity.

This allows each spectrum to be viewed as a histogram of a probability mass function (PMF) defined on the spectral range. Let  $\mathbf{p} = \{p_i\}_{i=1}^N$  and  $\mathbf{q} = \{q_i\}_{i=1}^N$  be the resulting PMFs of these two histograms. From information theory, a criterion called divergence can be used to measure the discrepancy between any two probability distributions. The spectral divergence,  $SD(\mathbf{p}, \mathbf{q})$ , can be defined as the divergence of the two PMFs formed from the two spectral signatures. This definition is given in (11)

$$SD(\mathbf{p}, \mathbf{q}) = L(\mathbf{p}; \mathbf{q}) + L(\mathbf{q}; \mathbf{p}). \quad (11)$$

The quantity  $L(\mathbf{p}; \mathbf{q})$  is the expected value of the log-likelihood ratio with respect to  $\mathbf{p}$  and is defined in (12)

$$L(\mathbf{p}; \mathbf{q}) = E \left[ \log \left( \frac{\mathbf{p}}{\mathbf{q}} \right) \right] = \sum_{i=1}^N p_i \log p_i / q_i. \quad (12)$$

This function is known as the Kullback-Leibler's discriminant or relative entropy function and is a nonsymmetric function. That is,  $L(\mathbf{p}; \mathbf{q})$  does not usually equal  $L(\mathbf{q}; \mathbf{p})$ . Nonetheless, the divergence is a symmetric form of the discrimination. The spectral divergence can be interpreted as a similarity measure between two spectra. The closer this measure is to zero, the more similar the two signatures are to each other. The values of the spectral divergence of the three signatures used in this experiment are given in Table I. The spectral divergence shows that the three signatures are similar to each other and thus should be difficult to distinguish from one another.

The three signatures were combined to form 550 mixed pixels. The abundance of the creosote leaves signature was set equal to 0% and the abundance

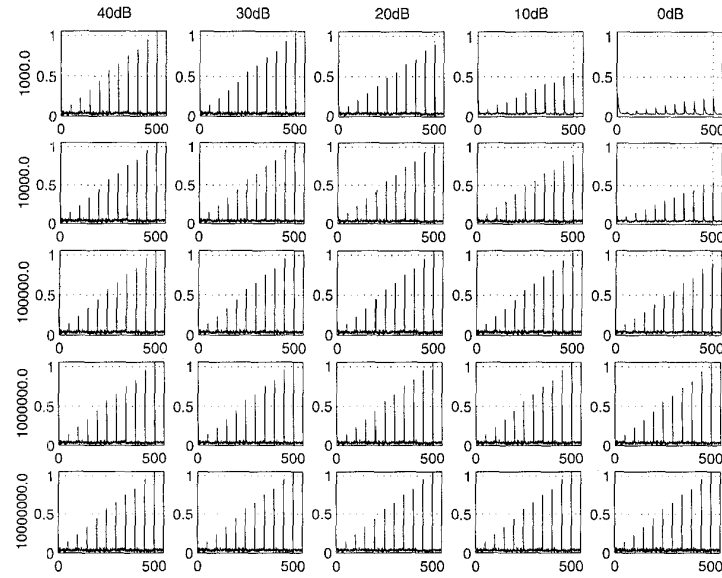


Fig. 2. Results of using simulated data based on Fig. 1.

TABLE I  
Values of Spectral Divergence of 3 Signatures, Creosote Leaves, Sage Brush, Black Brush in Fig. 1

	Creosote Leaves	Sage Brush	Black Brush
Creosote Leaves	0.0000	0.0554	0.0385
Sage Brush	0.0554	0.0000	0.0079
Black Brush	0.0385	0.0079	0.0000

TABLE II  
Values of Spectral Divergence of 4 Signatures, Treaded Vehicle, Wheeled Vehicle, Object 1, Object 2 in Fig. 3

	Treaded Vehicle	Wheeled Vehicle	Object 1
Treaded Vehicle	0.0000	0.0363	0.0430
Wheeled Vehicle	0.0363	0.0000	0.0092
Object 1	0.0430	0.0092	0.0000

of the other two signatures was set equal to 50%. Every 50th pixel of this sequence was replaced with a pixel that contains a non-zero abundance of the creosote leaves signature and the remaining abundance split evenly between the other two signatures. The abundance of the creosote leaves signature started at 10% for the 50th pixel, 20% for the 100th pixel and so on until the creosote leaves signature abundance in the 500th pixel reached 100%. White Gauss noise was added to each pixel to generate an SNR of 20 dB. The SNR was measured as defined in [5] as 50% of the reflectance divided by the standard deviation of the noise. This definition of SNR is used throughout this section.

The LUKF algorithm was run against the simulated data with  $\sigma_u^2$  and  $\sigma_v^2$  set at certain values. The value of  $\sigma_v^2$  was set to 1,000, 10,000, 100,000, 1,000,000, and 10,000,000. The value of  $\sigma_u^2$  was set such that the estimated SNR was 0, 10, 20, 30, and 40 dB. These represent the estimated SNR 20 dB below the actual SNR, the actual SNR, 10 dB above the actual SNR, and 20 dB above the actual SNR. The values of  $\sigma_u^2$  and  $\sigma_v^2$  were chosen to give a wide range of values of the parameters.

The results of these tests are shown in Fig. 2. This figure is set up such that each row is the results at a constant value of  $\sigma_v^2$  and each column is a constant value of  $\sigma_u^2$ . Each row is labeled with its corresponding value of  $\sigma_v^2$ . Each column is labeled with the SNR estimated by its corresponding value of  $\sigma_u^2$ . These plots show the effects of the values of  $\sigma_v^2$  and  $\sigma_u^2$  on the performance of the LUKF. The last two rows of Fig. 2 represent  $\sigma_v^2$  equal to 1,000,000 and 10,000,000, respectively, and show that the performance of the LUKF is affected little by the estimate of the SNR being off by either 20 dB above or below the actual SNR of the image. At these levels of  $\sigma_v^2$  the estimate of the SNR of the image can be as much as 20 dB deviation from the actual SNR of the image and the performance of the LUKF is not affected. Operation of the LUKF over this large range of SNR does not require the estimate to be exact. Fig. 2 does show that if  $\sigma_v^2$  is set too low, e.g.  $\sigma_v^2$  equal to 1,000, 10,000, the performance of the LUKF is affected by the value of  $\sigma_u^2$ . At these low values of  $\sigma_v^2$ , the LUKF is sluggish and slow to react to the sudden change in the abundance vector. The first two columns of Fig. 2 represent  $\sigma_u^2$  where the estimated SNR is 40 and 30 dB, respectively, and show that the values of  $\sigma_v^2$  have little affect on the

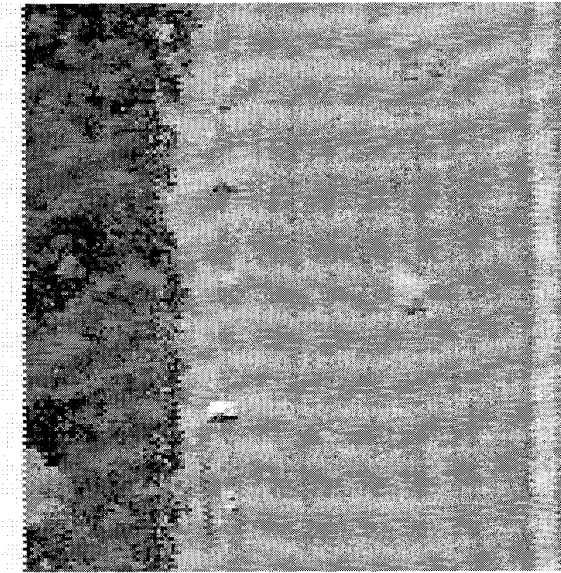


Fig. 3. Single band HYDICE scene.

performance of the LUKF. These results show that the LUKF can be used to estimate the abundance vector and perform subpixel classification, provided that  $\sigma_v^2$  and  $\sigma_u^2$  are properly chosen. These tests also show that the LUKF is stable for a large range of  $\sigma_v^2$  and  $\sigma_u^2$ . This is an important observation because it shows that the parameters can be set to these values and not have to be adjusted for each individual image. If  $\sigma_v^2$  is kept above 100,000, the performance of the LUKF is affected very little by changes in the actual SNR of  $\pm 20$  dB. This allows stable performance of the LUKF on hyperspectral data.

## B. Computer Simulations Using Radiances Directly Extracted from a HYDICE Scene

In Section IVA, computer simulations were conducted based on the three AVIRIS laboratory reflectance signatures used in [5] to demonstrate the capability of the LUKF in detecting abrupt abundance change in signatures. In this section, we run similar computer simulations based on radiances directly extracted from a real scene. The goal of this section is two-fold. One is to validate the results of Section IVA for real data. Another is to estimate the two noise variances,  $\sigma_v^2$  and  $\sigma_u^2$ , for real scenes which are used in Section V. Despite the experiments of this section based on a HYDICE scene shown in Fig. 3, the results can be also applied to the AVIRIS scene used in [11]. There are seven man-made targets shown in the scene, five vehicles, and two objects. The five vehicles are aligned vertically of which the first four on the top are treaded vehicles and the last one is a wheeled vehicle. Object 1 is at the top edge of the scene and Object 2 is located in the middle of the scene. All of these seven radiances were directly extracted from the HYDICE scene. However, for simplicity, only four signatures, the first treaded vehicle, the wheeled vehicle, object 1 and object 2 as shown in Fig. 4 are used for computer simulations.

Only three signatures, the first treaded vehicle, the wheeled vehicle and object 2 were combined to form 550 mixed pixels analogous to Section IVA. The abundance of the treaded vehicle signature was set equal to 0% and the abundance of the other two signatures was set equal to 50%. Every 50th pixel of this sequence was replaced with a pixel that contain a non-zero abundance of the treaded vehicle signature and the remaining abundance split evenly between the

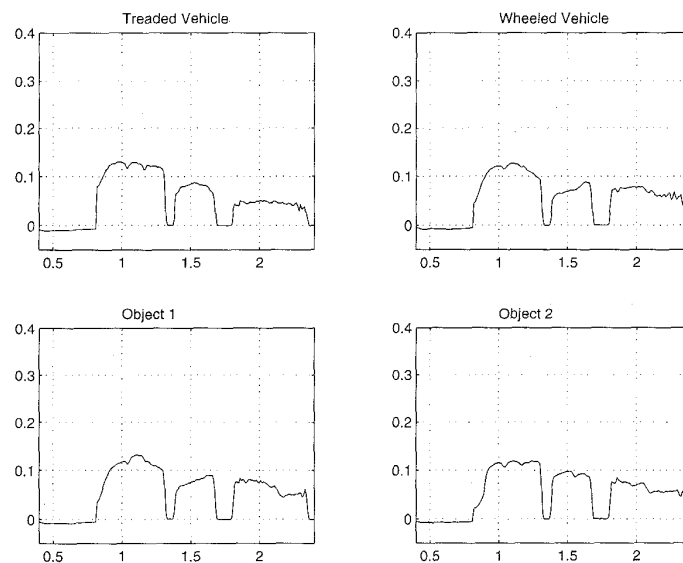


Fig. 4. Radiances of signatures, treaded vehicle, wheeled vehicle, Object 1, and Object 2 shown in Fig. 3.

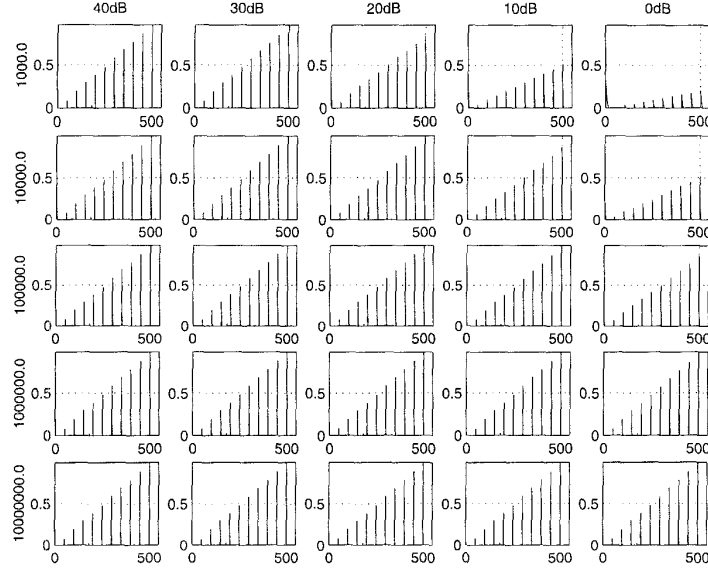


Fig. 5. Results using simulated data based on Fig. 4.

other two signatures. The abundance of the treaded vehicle signature started at 10% for the 50th pixel, 20% for the 100th pixel, and so on until the treaded vehicle signature abundance in the 500th pixel was 100%. Like Section IVA, white Gaussian noise was added to each pixel to generate SNR of 20 dB.

The LUKF algorithm was run against the simulated data with  $\sigma_u^2$  and  $\sigma_v^2$  set at certain values. The same values of  $\sigma_v^2$  and  $\sigma_u^2$  were used as in the previous section. The results of these tests are shown in Fig. 5 and are very similar to Fig. 2. It is set up as was Fig. 2 with each row representing the results at a constant value of  $\sigma_v^2$  and each column representing a constant SNR value and thus a constant value of  $\sigma_u^2$ . Each row and column are labeled with its corresponding value of  $\sigma_v^2$  and SNR level, respectively. These graphs also show that the values of the parameters  $\sigma_v^2$  and  $\sigma_u^2$  can have little affect on the performance of the LUKF if  $\sigma_v^2$  and  $\sigma_u^2$  are properly chosen. The last two rows of Fig. 5, have  $\sigma_v^2$  equal to 1,000,000 and 10,000,000, respectively, and show that the performance of the LUKF is affected little by the estimate of the SNR being off by either 20 dB above or below the actual SNR of the image. In analogy with Fig. 2, the first two columns of Fig. 5 represent  $\sigma_u^2$  with the estimated SNR being 10 and 20 dB above the actual SNR and show that the values of  $\sigma_v^2$  have little affect on the performance of the LUKF. But, when  $\sigma_v^2$  is set too low, e.g. 1,000, 10,000, the performance of the LUKF is affected by the values of  $\sigma_u^2$  in which case, the LUKF is sluggish and slow to react to the sudden change in the abundance vector. These tests also show that the LUKF is stable for a large range of  $\sigma_v^2$  and  $\sigma_u^2$  for real data and these parameters do not need adjustment for each individual

image. As long as  $\sigma_v^2$  remains above 10,000, the performance of the LUKF is not affected by changes in the actual SNR of  $\pm 20$  dB. This supports that the LUKF can be used for the following real data experiments and the performance will not be affected by noise fluctuations.

## V. HYPERSPECTRAL AND MULTISPECTRAL IMAGES

In this section we apply the LUKF to real hyperspectral and multispectral data. The results obtained in Section IV are used to set the parameters of the LUKF,  $\sigma_v^2$  and  $\sigma_u^2$ , to appropriate values. The values of  $\sigma_v^2$  was set to 1,000,000 and  $\sigma_u^2$  was set in such a manner that the estimated SNR was 20 dB. The LUKF, with these parameters, was applied to the HYDICE and SPOT data. The results of the LUKF are shown in Figs. 7–10.

### A. HYDICE Data

In this section the results of the LUKF when applied to HYDICE data is shown. The data used in this study were collected in Maryland in August 1995 with 210 bands with resolution 10 nm with spectral coverage from 0.4 to 2.5  $\mu\text{m}$  and a spatial resolution of approximately 0.78 m. A 160 by 160 pixel subimage was cropped from this data and the 180th band of this data is shown in Fig. 3. This figure shows a scene with trees along the left one-third, and a grass field in the right two thirds. The grass field also contains a road running along the right edge of the image. There are five vehicles located along the tree line and two objects. The five vehicles consist of four treaded vehicles in the upper half of the scene, and one wheeled vehicle in the lower half



TABLE III  
Values of Spectral Divergence of 7 Signatures, Five Vehicles, Two Objects in Fig. 6

	Vehicle 1	Vehicle 2	Vehicle 3	Vehicle 4	Vehicle 5	Object 1	Object 2
Vehicle 1	0.0000	0.0067	0.0076	0.0411	0.0363	0.0430	0.0766
Vehicle 2	0.0067	0.0000	0.0025	0.0522	0.0464	0.0532	0.0891
Vehicle 3	0.0076	0.0025	0.0000	0.0619	0.0592	0.0684	0.1086
Vehicle 4	0.041	0.0522	0.0619	0.0000	0.0066	0.0197	0.0679
Vehicle 5	0.0363	0.0464	0.0592	0.0066	0.0000	0.0092	0.0393
Object 1	0.0430	0.0532	0.0684	0.0197	0.0092	0.0000	0.0289
Object 2	0.0766	0.0891	0.1086	0.0679	0.0393	0.0289	0.0000

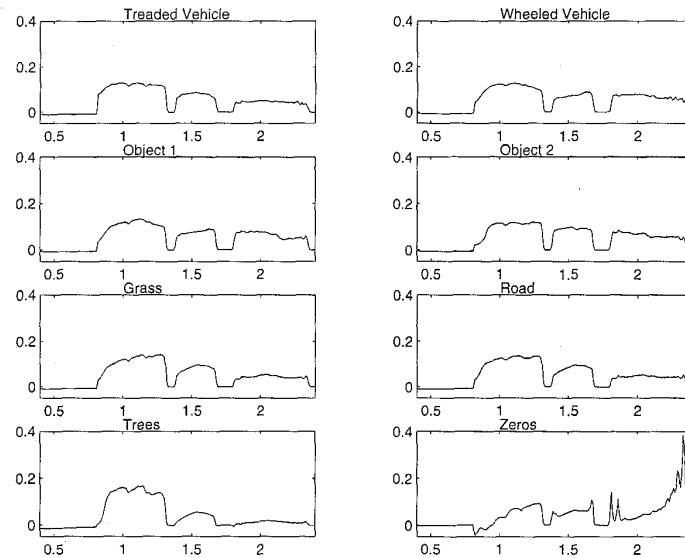


Fig. 6. Spectra of 8 signatures directly extracted from Fig. 3.

of the image. The size of the four treaded vehicles is approximately 4 m by 8 m and the size of the wheeled vehicle is 3 m by 6 m. The first object, Object 1, is at the top edge of the scene and the second, Object 2, is in the middle of the scene.

Eleven signatures that were generated were obtained by extracting pixels from the scene corresponding to different materials. The first eight consist of man-made objects. These include one signature for each of the five vehicles, one signature of each of the two types of objects, and a signature for the road. The next two signatures were natural background consisting of a signature for the grass field and a signature for the trees. The final signature consists of pixels that were zero vectors before the data was adjusted using the offset and gains for each band. This is because the first six pixels of each row (some rows may have the first seven pixels) of this HYDICE data were zero vectors and this signature was added to reduce the effects of these pixels. These zero pixels were a result of the data acquisition process and were not an actual part of the scene. The signatures for grass, trees, and road were also added to reduce the interfering effects of these materials. The

distance measure described in Section IVA, spectral divergence, was used to determine the similarity of these signatures. These distances are given in Table III. Since the signature for vehicle 1 has the smallest maximum distance from the other three treaded vehicles, it was used as the signature for the treaded vehicles. The eight signatures used for this test are made up of the signatures for vehicle 1, vehicle 5, object 1, object 2, the road, the grass field, the trees, and the zero vector. These signatures were used to form the signature matrix  $\mathbf{S}$  in (2) and are shown in Fig. 6.

Fig. 7 contains four images, each corresponding to the estimate of the signature abundance. These four images are labeled Treaded vehicles, Wheeled vehicle, Object 1, and Object 2. These four images show that the targets in each of the images were detected with little interference from the other signatures in the image. The image labeled Treaded vehicles clearly shows that the LUKF detected the first three treaded vehicles with little interference from the shadow area along the tree line. This interference is most likely caused by portions of the shadows of the treaded vehicles being included in the treaded

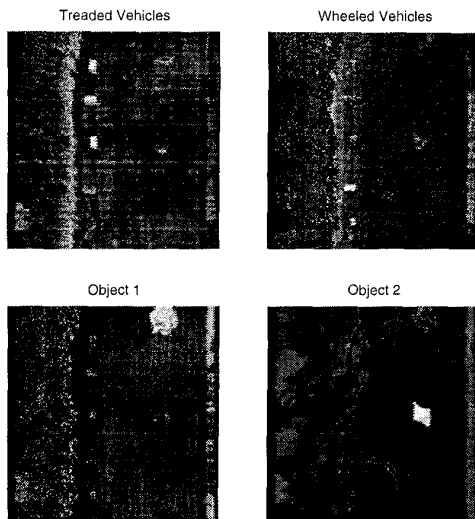


Fig. 7. Results of applying LUKF to HYDICE image scene.

vehicles signature. The fourth treaded vehicle was not detected by the LUKF, but this vehicle was detected as a wheeled vehicle. From Table III, the signature of the fourth treaded vehicle was much closer to the wheeled vehicle than any of the other treaded vehicles. The image corresponding to the wheeled vehicle shows that the wheeled vehicle was detected, again with the interference from the shadows of the trees. This image also shows that the fourth treaded vehicle was detected as a wheeled vehicle due to its similar signature. The image labeled by Object 1 shows that this object was detected with some interference from the road. Object 2 is detected with no interference. These four images all contain objects that are man-made and thus easy to distinguish from the natural background. The LUKF did accurately detect the four types of objects in the scene, with the exception of the fourth treaded vehicle. These four images show that the LUKF can be used to perform target detection and classification hyperspectral data.

#### B. SPOT Data

The multispectral data used to test the LUKF was collected by the SPOT system. The data consist of three bands. The first two bands are in the visible region of the electromagnetic spectrum and are referred to as band 1 ( $0.5\text{--}0.59\ \mu\text{m}$ ) and band 2 ( $0.61\text{--}0.68\ \mu\text{m}$ ). The third band is in the near infrared region of the electromagnetic spectrum and is referred to as band 3 ( $0.79\text{--}0.89\ \mu\text{m}$ ). The ground sampling distance of the SPOT system is 20 m. The data used are shown in Fig. 8 and represent a region of northern Virginia. These three bands are registered and combined to form an image cube. Each pixel in this image cube is a 3 by 1 vector with each component of the vector corresponding to one band



Fig. 8. 3 SPOT band images.

of the SPOT data. The experiment given below is a four-signature classification using a 3 band image.

The scene in Fig. 8 contains several buildings, bodies of water, highways, and secondary roads. These features were used as desired signatures for the signature matrix  $S$  in the LUKF. The signatures used in this experiment were directly extracted from the image and correspond to building, roads, water, and vegetation. The building signature was generated by averaging 9 pixels extracted from the scene that correspond to Falls Church High School. The road signature was generated by averaging 9 pixels extracted from the scene that correspond to Little River Turnpike. The water signature was generated by averaging 9 pixels extracted from the scene that correspond to the lake in the upper right of the image. Finally, the vegetation pixel was generated by averaging 9 pixels extracted from the scene that correspond to the Mill Creek Park. All four of these signatures were normalized and are shown in Fig. 9. The spectral divergence was used to determine the similarity of these signatures. These divergence values for the four signatures are given in Table IV. It shows that the road signature is very close to the water and

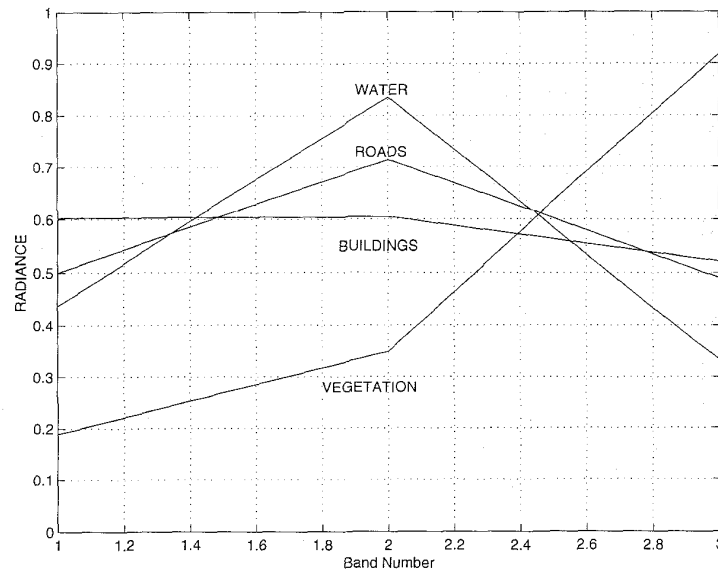


Fig. 9. Spectra of 4 signatures, roads, buildings, water, and vegetation directly extracted from SPOT images.

TABLE IV  
Values of Spectral Divergence of 4 Signatures, Roads, Buildings, Water, Vegetation in Fig. 9

	Building	Roads	Water	Vegetation
Building	0.0000	0.0228	0.1223	0.4993
Roads	0.0228	0.0000	0.0498	0.5020
Water	0.1223	0.0498	0.0000	0.7922
Vegetation	0.4993	0.5020	0.7922	0.0000

building signatures, and both the building and road signatures are similar.

Fig. 10 shows the results of the estimated abundance using the LUKF. The four images in Fig. 10 were compared with a map of the region, shown in Fig. 11, which shows the buildings, roads, and bodies of water in the scene. The image labeled as Buildings shows where there are high levels of abundance of the building signature. This image clearly shows the buildings in the scene were detected. The image labeled as Roads shows where there are high levels of abundance of the road signature. The estimate of the abundance generated by the LUKF not only revealed the major highway, but also the secondary and residential streets in the region. Even the turn and culdesacs of the residential streets can be seen in this image. The large areas of high abundance of roads that occur around buildings, represent parking lots. The image labeled as Water shows where there are high levels of abundance of the water signature. This image clearly indicates the lake located in the area at the top of the image. In addition, a small pond is also picked up in the lower left of the image. The final image, labeled as Vegetation, shows where there are high levels of the vegetation signature. This image shows the large areas of high levels of

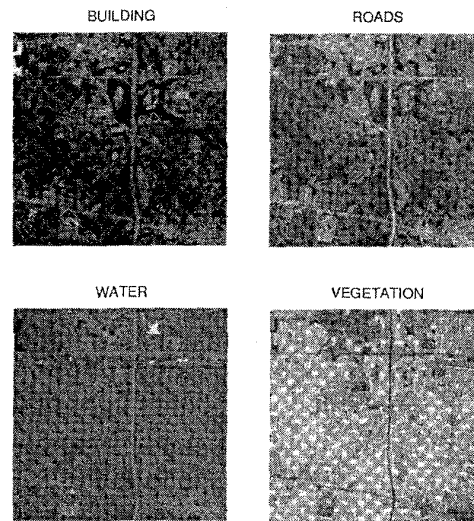


Fig. 10. Results of applying LUKF to SPOT images.

vegetation in almost all areas of the region. The map reveals many parks in the region. The comparison of this image to the map confirms that the large areas of high levels of vegetation correspond to the parks and residential areas in the region. The dark areas in the images represent low levels of vegetation that correspond to areas where building, roads, parking lots or bodies of water are located in the previous images. These four images show that the LUKF can also be used to perform image classification on multispectral data.

## VI. CONCLUSION

This paper presents a new approach, called LUKF which incorporates the linear mixture model into the



Fig. 11. Map of SPOT data used in experiment.

Kalman filtering. It implements the widely used linear unmixing method in a Kalman filtering fashion so that it can be used for abundance change detection, signature estimation, and subpixel classification. The performance of the LUKF is demonstrated through simulated and real data. As shown in the experiments, the LUKF can effectively perform subpixel analysis and detect abundance change.

#### ACKNOWLEDGMENTS

The authors would like to thank the Spectral Information Technology Applications Center for providing the hyperspectral data set used for experiments in this paper. They also thank Dr. Shin-Yi

Hsu with Susquehanna Resources and Environment, Inc. for providing SPOT data.

#### REFERENCES

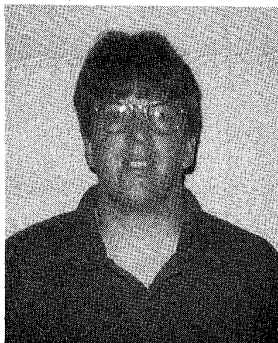
- [1] Vane, G., and Goetz, A. F. H. (1994) Terrestrial imaging spectroscopy. *Remote Sensing of Environment*, **24** (1994), 1–29.
- [2] Goetz, A. F. H., and Boardman, J. W. (1989) Quantitative determination of imaging spectrometer specifications based on spectral mixing models. In *Proceedings of IEEE Geoscience and Remote Sensing*, 1989, 1036–1039.
- [3] Adams, J. B., and Smith, M. O. (1986) Spectral mixture modeling: A new analysis of rock and soil types at the Vikign lander 1 suite. *Journal of Geophysical Research*, **91** (1986), 8098–8112.
- [4] Shimabukuro, Y. E., and Smith, J. A. (1991) The least-squares mixing models to generate fraction images derived from remote sensing multispectral data. *IEEE Transactions on Geoscience and Remote Sensing*, **29** (1991), 16–20.
- [5] Harsanyi, J., and Chang, C.-I (1994) Hyperspectral image classification and dimensionality reduction: An orthogonal subspace projection approach. *IEEE Transactions on Geoscience and Remote Sensing*, **32** (1994), 779–785.
- [6] Brumbley, C., and Chang, C.-I (1997) A Kalman filtering approach to hyperspectral image classification. In *Proceedings of the Conference on Information Sciences and Systems*, The Johns Hopkins University, Baltimore, MD, Mar. 19–21, 1997, 179–184.
- [7] Zhao, X. (1993) Subspace projection to multispectral/hyperspectral image classification using linear spectral mixture modeling. M.S. thesis, Department of Electrical Engineering, University of Maryland Baltimore County, MD, 1993.
- [8] Kalman, R. E. (1960) A new approach to linear filtering and prediction problems. *ASME Journal of Basic Engineering*, (1960), 95–108.
- [9] Haykin, S. (1996) *Adaptive Filtering Theory* (3rd ed.). Englewood Cliffs, NJ: Prentice-Hall, 1996.
- [10] Chang, C.-I An application of oblique subspace projection approach to hyperspectral image classification. To be submitted.
- [11] Brumbley, C. (1998) An unsupervised linear unmixing Kalman filtering approach to abundance detection, signature estimation and classification. Ph.D. dissertation, Department of Computer Science and Electrical Engineering, University of Maryland Baltimore County, Baltimore, MD, May 1998.



**Chein-I Chang** (M'87—SM'92) received his B.S., M.S. and M.A. degrees from Soochow University, Taipei, Taiwan, 1973, the Institute of Mathematics at National Tsing Hua University, Hsinchu, Taiwan, 1975 and the State University of New York at Stony Brook, 1977, respectively, all in mathematics, and M.S. and M.S.E.E. degrees from the University of Illinois at Urbana-Champaign in 1982, respectively, and Ph.D. in electrical engineering from the University of Maryland, College Park in 1987.

He was a visiting Assistant Professor from January 1987 to August 1987, Assistant Professor from 1987 to 1993, and is currently an Associate Professor in the Department of Computer Science and Electrical Engineering at the University of Maryland Baltimore County. He was a visiting specialist in the Institute of Information Engineering at the National Cheng Kung University, Tainan, Taiwan from 1994–1995. His research interests include information theory and coding, signal detection and estimation, multispectral/hyperspectral image processing, neural networks, pattern recognition.

Dr. Chang is a member of SPIE, INNS, Phi Kappa Phi, and Eta Kappa Nu.



**Clark M. Brumbley** received his B.S.E.E. degree from Old Dominion University, Norfolk, VA, 1985 and M.S.E.E. and Ph.D. from the University of Maryland Baltimore County in 1993 and 1998, all in electrical engineering.

He is currently a Senior Electronic Engineer for the Department of Defense at Ft. Meade, MD. His research interests include signal detection and estimation and multispectral/hyperspectral image processing.

Dr. Brumbley is a member of Tau Beta Pi, Eta Kappa Nu, and Sigma Xi.